LAWRENCE
LIVERMORE
NATIONAL
LABORATORY

LLNL-CONF-405081

The Gemini Planet Imager: From Science to Design to Construction

B. Macintosh, J. R. Graham, D. Palmer, R. Doyon, J. Dunn, D. Gavel, J. Larkin, B. Oppenheimer, L. Saddlemyer, A. Sivaramakrishnan, J. K. Wallace, B. Bauman, D. Erickson, C. Marois, L. Poyneer, R. Soummer

July 2, 2008

SPIE Astronomical Instrumentation
Marseille, France
June 23, 2008 through June 28, 2008

Disclaimer

The Gemini Planet Imager: from science to design to construction

Bruce A. Macintosh[*ab], James R. Graham[ac], David W. Palmer[ab], René Doyon[d], Jennifer Dunn[h], Donald T. Gavel[ae], James Larkin[af], Ben Oppenheimer[g], Les Saddlemyer[h], Anand Sivaramakrishnan[ag], J. Kent Wallace[ai], Brian Bauman [ab], Darren A. Erickson[h], Christian Marois [abh], Lisa A. Poyneer [ab], Remi Soummer [ag]

[a]NSF Center for Adaptive Optics

[b]Lawrence Livermore National Laboratory, 7000 East Ave., Livermore, CA 94551

[c]Department of Astronomy, University of California at Berkeley, Berkeley, CA 94720

[d]Universite de Montreal, Department de Physique, Montreal, QC, H3C 3J7, Canada

[e]UC Santa Cruz, 1156 High Street, Santa Cruz, CA

[f]Department of Physics and Astronomy, UC Los Angeles, Los Angeles, CA 90095

[g]Department of Astrophysics, American Museum of Natural History, New York, NY 10024

[h]Herzberg Institute of Astrophysics, 5071 West Saanich Road, Victoria, BC V8X 4M6

[i]Jet Propulsion Laboratory, California Institute of Technology, Pasadena, CA 91109

[j]Immervision, 2020 University, Suite 2420, Montreal, QC H3A 2A5, Canada

ABSTRACT

The Gemini Planet Imager (GPI) is a facility instrument under construction for the 8-m Gemini South telescope. It combines a 1500 subaperture AO system using a MEMS deformable mirror, an apodized-pupil Lyot coronagraph, a high-accuracy IR interferometer calibration system, and a near-infrared integral field spectrograph to allow detection and characterization of self-luminous extrasolar planets at planet/star contrast ratios of 10^{-7}. I will discuss the evolution from science requirements through modeling to the final detailed design, provide an overview of the subsystems and show models of the instrument's predicted performance.

Keywords: Adaptive optics, coronagraph, high-contrast, MEMS, integral field spectrograph, extrasolar planet

1. INTRODUCTION

1.1 Introduction to instrument

In the past decade, the study of extrasolar planets has progressed enormously, from a handful of detections to a rich taxonomy of solar systems. For the brightest and proportionally largest transiting planets, it is now possible to obtain spectroscopic information. Nonetheless, our knowledge is partial and the revolution is incomplete. Doppler techniques are only slowly progressing past the 5 AU boundary that marks the start of the giant planet region in our own solar system. Spectra, when obtained, are generally of low signal-to-noise ratio, and their comparison to models complicated by the effects of stellar irradiation.

Direct imaging of extrasolar planets is one of the next major steps in the field. The Gemini Planet Imager (GPI) is one major effort towards that goal. GPI is designed for near-infrared imaging and spectroscopy of young (10-1000 Myr), massive (1-10 M_J) self-luminous planets. GPI's direct coronagraphic images will be sensitive to planets in wide orbits, inaccessible to Doppler techniques. It will be capable of obtaining moderate resolution (R~10-100) of detectable planets, allowing their temperature and gravity to be measured. In this paper, we describe the scientific requirements of such an instrument, outline the GPI design, and present simulations of its performance

* macintosh1@llnl.gov

1.2 Scientific requirements

A true analog of Jupiter would have a contrast (flux ratio relative to its parent star) of 10^{-9}. Such contrasts are beyond the reach of any ground-based instrument on a 8-10m telescope. However, younger planets are significantly more luminous. Early models[1] predicted that a 10 million year old Jupiter-mass planet would have a contrast relative to a solar-type star of 10^{-7}. This is within the reach of even current adaptive optics systems, albeit at wide radii, and several extensive searches for such planets at 30 AU+ separations have been carried out[2].

For a next-generation instrument, it is desirable to significantly exceed this contrast for two reasons. First, young stars are naturally rare; if planets can be detected at greater ages, a larger sample of targets are accessible. Crudely, if the luminosity of a planet scales as age squared, increasing the contrast by a factor of 100 will increase the number of detected planets by a factor of ten. Second, there is considerable uncertainty in the properties of the youngest planets. Early models[1] assumed (for computational reasons) a "hot start" – an gradual and isentropic condensation of a gas and dust cloud into a planetary embryo which retains almost all of the released gravitational potential energy. More recent models that assume planets assemble through a runaway accretion process[3] predict much lower temperatures, luminosities, and near-infrared fluxes at the youngest ages (though older planets essentially forget their initial conditions.) The observable brightness of such a planet also depends on highly uncertain atmospheric structure and physics, particularly the properties of clouds. As a result of this uncertainty, it is desirable to obtain as high a contrast as possible given the fundamental limits of atmospheric and AO interactions GPI has been designed for a broadband contrast of ~10^{-7} on a I=6 mag. target. Since planet contrast is almost completely determined by effective temperature (planet radius is nearly independent of mass) this can be thought of as a minimum detectable planet temperature, ~300 K for a solar-type target.

Existing direct imaging surveys have good sensitivity (depending on the model uncertainties discussed above) for planets at separations beyond 30 AU. To cover a significant range of planetary phase space, a direct planet imager should be capable of seeing planets from ~5 AU. For a target sample of 1000 stars of age below 2 billion years, the median target distance will be 40 pc and hence the desired inner working angle is ~0.13 arc seconds.

Once planets have been discovered, significant scientific return will come from their spectral characterization. Spectral information can also be used to distinguish planets from artifact speckles. The ideal science instrument, therefore, is an imaging or "integral field" spectrograph (IFS.) The highest possible spectral resolution is always desirable, but practical considerations constrain this – multiple high-resolution spectra will fill the available detector, and too high a resolution will also cause detector read noise to limit signal-to-noise ratio in the final detection. In other words, there is a trade between final field of view and spectral resolution. We carried out extensive simulations to determine the lowest acceptable spectral resolution for planet characterization and decided on R~45, where $R=\Delta\lambda/\lambda$ is the resolution per two spectral pixels.

Other requirements are given in Table 1. For maximum sensitivity, particularly with post-processing stages that will involve shifting, rotating and resampling, images should be Nyquist or better sampled. The whole near-IR range should be exploited up through the range where thermal background will be prohibitive. Polarimetry will be a powerful technique for characterization of circumstellar dust disks and should be incorporated. Finally, planet properties (photometric and astrometric) must be measured with high enough precision.

Table 1: Scientific requirements on the Gemini Planet Imager

Property	Requirement Value	Notes
Detectable planet contrast.	10^{-7}	1 MJ @ 70 Myr age
Inner working angle	0.13 arcseconds	5 AU at 40 pc.
Spectral resolution	R ~ 45	Per two detector pixels
Wavelength coverage	1-2.4 μm	Standard *YJHK* bands
Instrument modes	Integral field spectrograph and imaging dual-channel polarimeter	Planet and dust disk characterization
Spatial sampling	0.014 arcseconds per pixel	Nyquist sampled at *J* band
Field of view	2.8 arcseconds	Desired for studies of dust disks

2. INSTRUMENTAL REQUIREMENTS AND CONTRAST DESIGN

The next step in an instrument process is translating these into lower-level functional and performance requirements on the instrument itself. In many cases this process is straightforward, but in the case of a high-contrast imager, the relationship is more complicated. Contrast is determined not by simple metrics like Strehl ratio or RMS WFE but by a variety of factors. As noted by many authors, residual atmospheric speckle noise is rarely the limiting factor in contrast for current systems – quasi-static speckles, evolving on timescales of minutes or hours, from internal aberrations sources always dominate. Some of these add independently (e.g. different sources of quasi-static wavefront error), usually linearly rather than in quadrature since final image intensity is already the square of the electric fields. Other terms connect in a more complicated way. For example, the local spatial image intensity variance due to quasi-static pinned speckles from residual wavefront phase errors is the product of the local electric field due to residual diffraction (the square root of the image intensity the coronagraph would produce with a perfectly flat wavefront) and the local electric field due to quasi-static aberrations (the absolute value of the Fourier transform of the phase, or the square root of the intensity the speckle halo would have with a perfect coronagraph.)[4] These cross terms are particularly significant in the chromaticity of the point spread function, a key term for multi-wavelength speckle suppression.

We dealt with this process through several tools. The first guiding principal was to set every major independent contrast term to a value of the same order of magnitude as the final target contrast. For example, considering only photon noise would imply that the residual diffraction from the coronagraph need only be lower than the intensity of scattered light from the atmospheric halo ($\sim 10^{-5}$ contrast), but this is not the case – since the diffraction halo cross-couples with the quasi-static errors, it must be comparable to the intensity of those speckles which in turn must be comparable to the target performance ($\sim 10^{-7}$ contrast). This also insures that the cross-product terms do not degrade contrast by more than a factor of ~2.

The second guiding principal was that atmospheric and quasi-static speckle errors should be comparable in a typical 1-hour science exposure, so that GPI is limited by the atmosphere rather than its internal optics. This is a very challenging specification, but on bright stars it may be somewhat underspecified – atmospheric speckles are easily suppressed by SSDI imaging by a factor of 100 or more, but quasi-static speckles are generally more chromatic and only attenuated by a factor of 2-10. Still, at these levels of performance, GPI will achieve the photon noise limit on typical (H>5 mag.) science targets.

The third guiding principal is to minimize chromaticity of all error sources, to improve the performance of SSDI post processing. This includes the obvious chromaticity sources (transmissive optics) but also more esoteric sources such as chromatic beam walk and Fresnel propagation.

The fourth principal is to invest in the best quality optics practical. Many terms in the contrast budget (Fresnel propagation, beam walk, time evolution of NCP errors, etc.) derive from the quality of individual optical surfaces – and some of these (Fresnel effects) are fundamentally uncorrectable and set the performance floor for GPI.

To determine the actual values for requirements, a hierarchy of modeling tools were used. The original conceptual design used an analytic contrast error budget spreadsheet. Some terms in this error budget were calculated from first principals, others (Fresnel/Talbot effects) evaluated numerically to determine scaling laws for the spreadsheet.

2.1 Fresnel and Talbot effects

As the GPI design progressed, these values were updated using detailed simulations. A particularly important class of aberrations are Fresnel propagation terms – in particular, the Talbot effect. Briefly, in the Talbot effect, a pure phase aberration on an optical surface "mixes" between phase and amplitude as light propagates. In a collimated beam, this oscillation occurs over a distance $\tau_L = 2\Lambda^2/\lambda$ where Λ is the aberration spatial period and λ the wavelength of the light. Figure 1 illustrates this effect.

This process is particularly important to high-contrast AO imagers. Phase aberrations (if they are sensed correctly) can be corrected with a single deformable mirror through simple phase conjugation, but amplitude aberrations cannot; to correct for amplitude errors one must measure amplitude and either apply a "half-dark-hole" algorithm[5 6] which cancels the amplitude-induced speckles over only part of the field of view, or operate with multiple DMs, neither of which are practical in a ground-based system. In addition, these aberrations are inherently chromatic. During preliminary design, we evaluated their effects using a analytic Talbot calculation. The Talbot approximation assumes optics are located in a collimated beam, so elements were grouped into several subsets and projected into their equivalent conjugate height in

the collimated space above the telescope. Figure 2 shows the result of this analysis for each individual optic, while Table 2 gives the values of optical surface quality used. As expected, optics close to focus are the most critical.

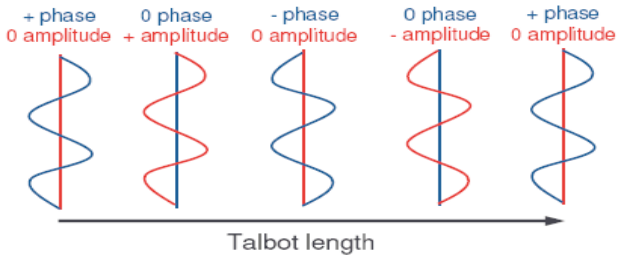

Figure 1: An illustration of the Talbot effect showing the phase (blue) and amplitude (red) of the wavefront as it propagates.

Table 2: GPI optical surface aberrations with corresponding conjugated planes. Individual optics are combined into groups for a Talbot analysis.

Surface	Grouped conj. altitude (km)	True conj. altitude (km)	0-4λ/D^{-1} RMS WFE (nm RMS)	4-22λ/D^{-1} RMS WFE (nm)	Amplitude error (% RMS)
ADC01*	250	250	7	1.4	0.14
ADC02*	110	110	7	1.4	0.14
Window*	73.2	55.7	2.5	0.5	0.1
Ellipse		73.2	5	1	0.1
OAP3		63.3	5	1	0.1
OAP4		58.7	5	1	0.1
Folding flat		67.7	2.5	0.5	0.1
Beam-Splitter*	40	40	7	1.4	0.14
OAP1	27	27	5	1	0.1
OAP2		27.4	5	1	0.1
M3	0	17.6	5	14	0.3
MEMs		0	-	-	-
M1		0.1	5	50	0.3
M2		0	5		0.3

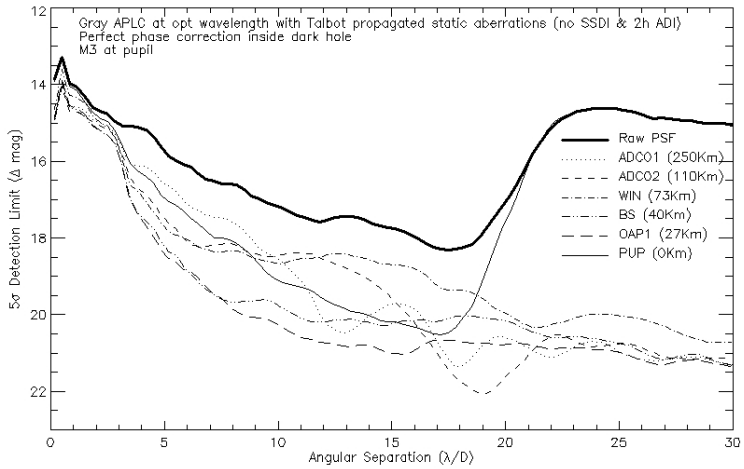

Figure 2: Contrast loss for each optics group in the Talbot analysis. Note that this simulation was carried out earlier in the GPI design using a less-capable coronagraph, which degraded performance in the 5-10 λ/D range.

In the subsequent Critical Design phase, this analysis was replaced with a sophisticated optic-by-optic Fresnel simulation. Results from this are presented below (Section 9) and described extensively in a companion paper[7].

3. INSTRUMENT OVERVIEW AND LIGHT PATH

GPI consists of six major subsystems. The adaptive optics (AO) system controls the wavefront errors induced by the atmosphere, telescope, and GPI's own optics. The coronagraph masks control the diffraction of coherent starlight. The calibration interferometer (CAL) is one of the most unique features – a post-coronagraphic wavefront sensor, it exploits the optical properties of the coronagraphic process to sense the wavefront at the focal plane occultor, the key location. The cryogenic Integral Field Spectrograph (IFS) is the only science instrument. Finally, an opto-mechanical superstructure (OMSS) supports all the subsystems and components. Top-level software[8] coordinates the operation of the instrument and interfaces to the observatory.

Figure 3 shows the light path. Light enters the instrument through a window; the instrument enclosure is overpressurized with dry clean air to protect optical surfaces. A deployable atmospheric dispersion corrector aligns different wavelengths of light in both the coronagraphic focal plane and (equally crucially) on all the GPI internal optics, so that the light seen by wavefront sensors acquires the same aberrations as the light in the science path. A variety of calibration sources can be injected into the input focus. To achieve good coronagraphic images, these light sources must produce very uniform illumination of the pupil, which will require sending the light through a very small pinhole and massively overfilling the GPI optics. As a result, we require an extremely bright light such as a supercontinuum source with a power of several mw in a single-mode fiber.

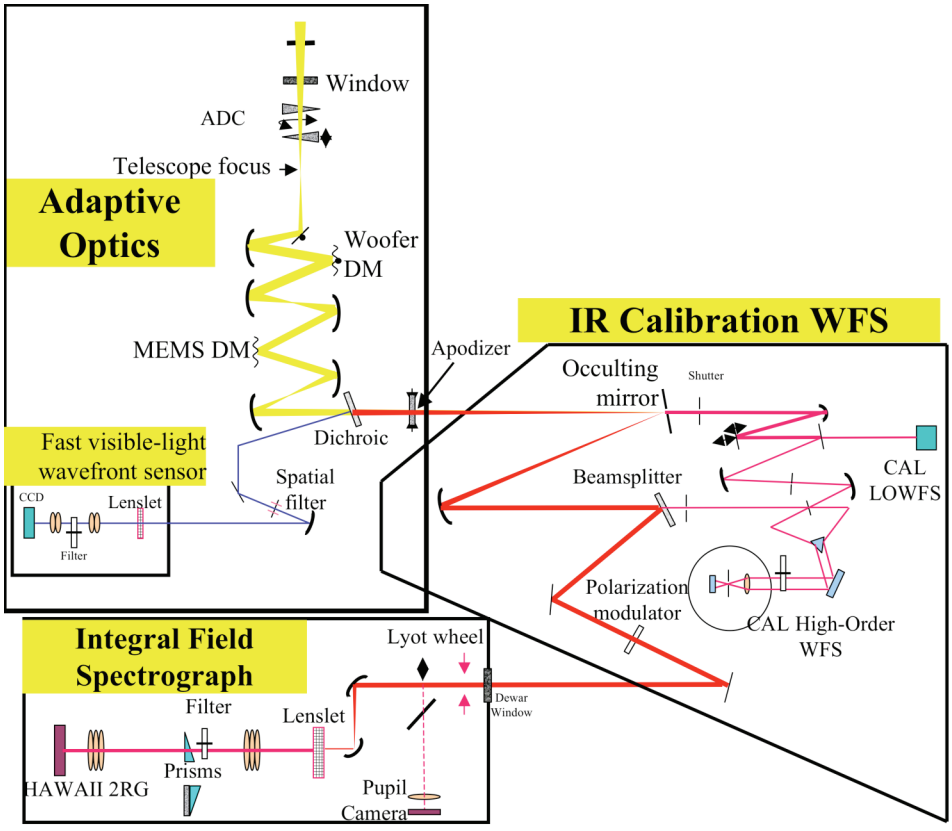

Figure 3: GPI Schematic design.

4. AO SUBSYSTEM

4.1 Introduction and properties

GPI's adaptive optics system exists to control both dynamic wavefront errors (atmospheric phase errors) and to implement correction of slowly-varying static wavefront errors reported by the CAL system. It is a two-stage AO system with a MEMS deformable mirror and a conventional piezo-electric DM operating in a woofer-tweeter correction. The visible-light wavefront sensor incorporates a spatial filter[9] to prevent aliasing and operates in the red 700-900 nm regime where the spatial filter performance is optimal. Wavefronts are reconstructed using an optimized Fourier modal algorithm[10], with a possible extension to a predictive control being studied[11]. The AO system is mounted on a custom aluminum optical bench (Figure 4).

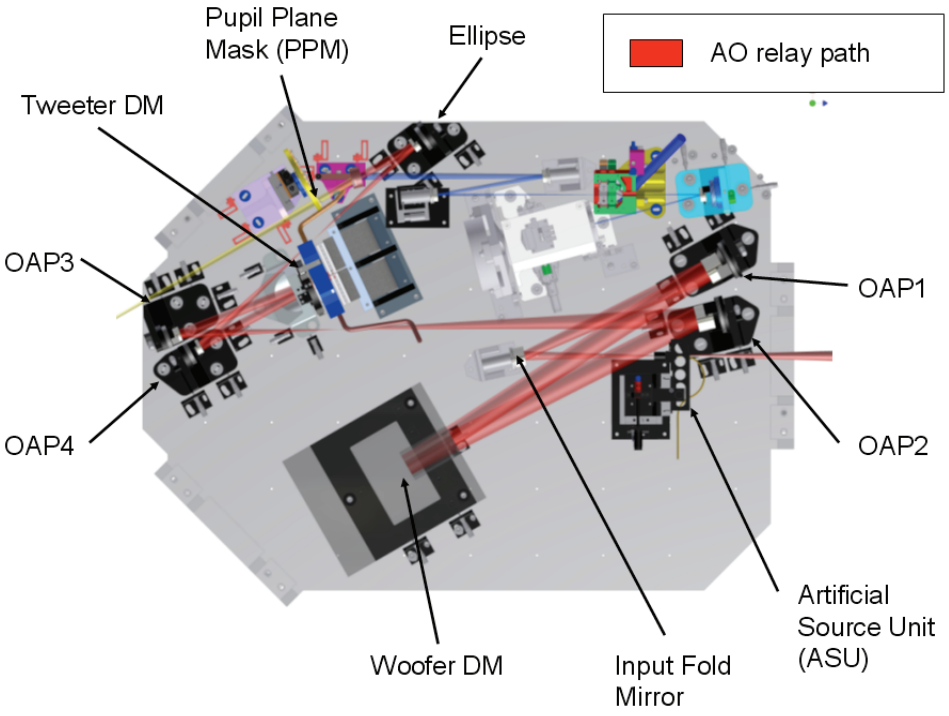

Figure 4: Layout of the AO relay components on the GPI AO optical bench. The blue path in the upper right shows the light path to the wavefront sensor. Total size is approximately 1 meter in width.

4.2 CCD

The original GPI design was optimized for very fast performance (2-2.5 kHz frame rate) to maximize performance on bright stars (I<5 mag.) Very few CCDs could achieve these rates for GPI's 44x44 subaperture geometry; the most practical options are the Lincoln Laboratory CCID-18 and the E2V CCD-50. However, it was recognized during science modeling that most surveyed targets will be dimmer than this, and that the optimized and/or predictive Fourier controller reduces the need for raw temporal bandwidth. A slightly slower but lower-noise CCD was therefore an attractive option. One such device is the new CCID-56 device, incorporating on-chip JFET amplification to achieve noise of 1-3 electrons.

Table 3: Properties of CCDs studied for GPI.

Property	**LL CCID-56B**	LL CCID-18	E2V CCD-50
Format	**160 × 160**	128 × 128	128 × 128
Outputs	**20**	16	16
Readnoise (e^- rms)	**1**	9-12	7-10

Property	**LL CCID-56B**	LL CCID-18	E2V CCD-50
Maximum pixel rate per output (MHz)	**1.5**	2.5	4
Maximum frame rate (full frame) (Hz)	**890**	2000	2500
Maximum frame rate (88 rows) (Hz)	**1500**	2900	3500
Readout time (GPI geometry) (μs)	**640**	345	412
Average QE, 700-900 nm	**85%**	65%	

We used an analytic AO PSF prediction code to compare the science capabilities of the two LL CCDs. Figure 5 shows the photon noise from the residual atmospheric halo (the fundamental limit) for a variety of star magnitudes. As can be seen, the fast but noisy CCID-18 only shows a performance advantage for targets brighter than *I*=6 mag, while the CCID-56 opens up significant science reach at *I*=9 mag.

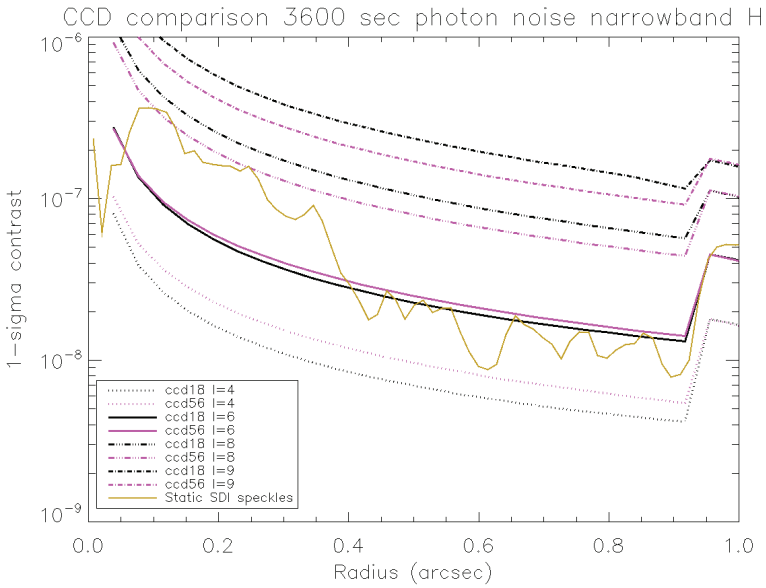

Figure 5: PSF comparison between the CCID-18 and CCID-56 devices for *I* = 4, 6, 8, and 9 mag. targets. Also shown is the contrast level set by static speckles. The static speckle simulation used the PDR coronagraph design—the improved broadband CDR coronagraph strongly reduces speckle noise from 0.2–0.4 arc seconds. The CCID-56 performs better on all but the brightest targets.

4.3 MEMS deformable mirror status

The most developmental component of GPI is its deformable mirror. To fit a ExAO system with N=44 actuators into a Gemini instrument envelope, MEMS DM technology is absolutely required. We have funded development of a 64x64 MEMS DM at Boston Micromachines[12]. The first prototypes mirrors are now available. These achieve 4 microns (surface) overall stroke and >1 micron inter-actuator stroke. Typical surface quality is excellent, with RMS high-frequency surface figure (actuator print-through and actuator-scale scalloping) of 4-10 nm RMS. The devices do show 2-4 microns (PV) overall curvature, primarily focus, but this can easily be corrected with GPI's woofer or by refocusing the Gemini telescope. Actuator yield on the first devices has been reduced by wire-bonding errors and defects in the connector spacers used with the large flex cables. Mounting the DM on GPI is discussed in a separate paper[13].

5. APODIZED-PUPIL LYOT CORONAGRAPH

GPI's primary diffraction control system is an apodized-pupil Lyot coronagraph (APLC)[14]. This combines a classic Lyot coronagraph (hard-edged focal-plane occultor and undersized pupil-plane Lyot stop) with a moderate apodization function, matched to the occultor geometry to almost completely attenuate the light within the original pupil diameter. In GPI's case, the apodizers are in an pupil-plane-mask (PPM) wheel located on the adaptive optics bench. The occultors are reflective in design, with the on-axis light sent through a hole while off-axis science light is reflected; these occultors

are mounted in a selection wheel in the Calibration subsystem. Finally, the cryogenic Lyot stops are located in a wheel inside the Integral Field Spectrograph. Since GPI will normally operate with the Gemini Cassegrain-focus sky derotator deactivated, the Lyot stops cannot independently rotate to track the telescope orientation; instead, a number of masks corresponding to different instrument orientations are provided.

The APLC coronagraph does have some inherent chromaticity, since the occultor size in λ/D units will only match the apodizer design at one individual wavelength. The original GPI coronagraph design at PDR had moderately significant chromaticity, with contrast varying by a factor of 5 across most of *H* band. The GPI APLC is optimized for broad-band performance at a slight cost to inner working angle; the hard-edged occultor masks have a diameter of 5.6 λ/D and the masks are numerically optimized only for performance from a radius of 4.8-22 λ/D.

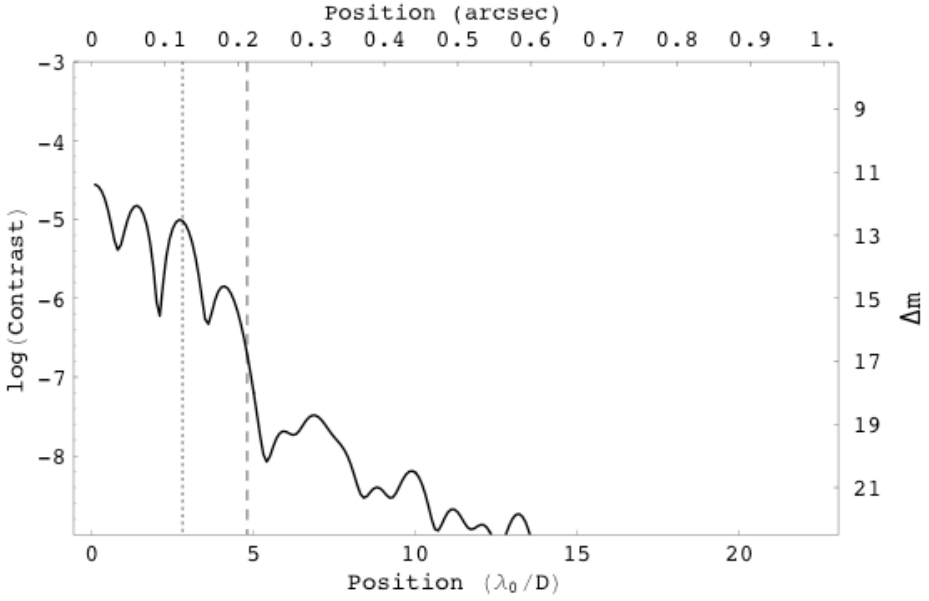

Figure 6: Contrast vs. radius for the GPI apodized-pupil Lyot coronagraph at 1.6 μm, for a perfect case with no wavefront error.

GPI's apodizers will also incorporate a grid pattern to generate astrometric reference spots – ghost images of the primary star – in the final PSF[15 16].

5.1 Manufacturing

Although the GPI apodizer functions are moderate (~5% transmission at the edge with no sharp features), they are still very difficult to manufacture. We have evaluated several technologies for this purpose. Electron-sensitized HEBS glass was one attractive option, since it can accommodate continuous ranges of transmission. However, HEBS glass is not commercial used at IR wavelengths and limited experience exists. In addition, the process of writing a HEBS pattern induces a significant wavefront error. From the Kramers-Kronig relation this can be estimated for HEBS glass and is quite strong in the near-infrared,, with ~0.8 microns OPD for a OD=1.5[17]. Although this could be corrected using GPI's deformable mirrors, such a large non-common-path wavefront error would drive the wavefront sensor spots out of their quadcell linear range and degrade AO performance.

Instead, the baseline technology is to manufacture these will be chromium microdots deposited on glass in a binary halftone approximation of the target apodizer function. The required geometry is not simply set by geometric or even Fraunhofer optics, though. Individual dot sizes are 1-2 μm, so electromagnetic effects become important[18]. We are writing a series of calibration targets and will measure their transmission in the on-axis zero order using a Brookhaven National Laboratory synchrotron light source.

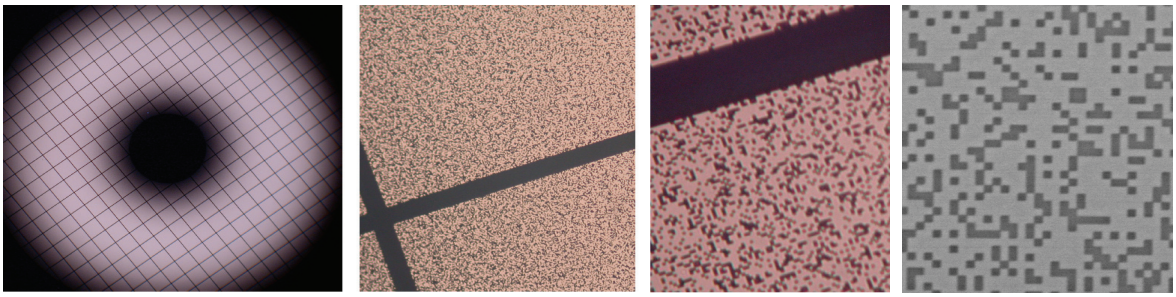

Figure 7: Prototype apodizer manufactured with chromium microdots on a square substrate, viewed at increasing magnification.

Prototypes of these masks have been tested at the UC Santa Cruz Laboratory for Adaptive Optics (LAO) and achieved $>10^7$ contrast[19].

6. CAL INTERFEROMETER

As discussed above, a key to high-contrast imaging is removing the residual static wavefront errors, insuring that the time-averaged phase at the coronagraphic occultor is flat. For GPI, the requirement is 1 nm RMS wavefront error at mid spatial frequencies (4-22 cycles/aperture.) The primary visible-light Shack-Hartmann AO WFS cannot necessarily achieve this, due chromaticity, non-linearity, and to non-common-path optical errors which will likely evolve with time.

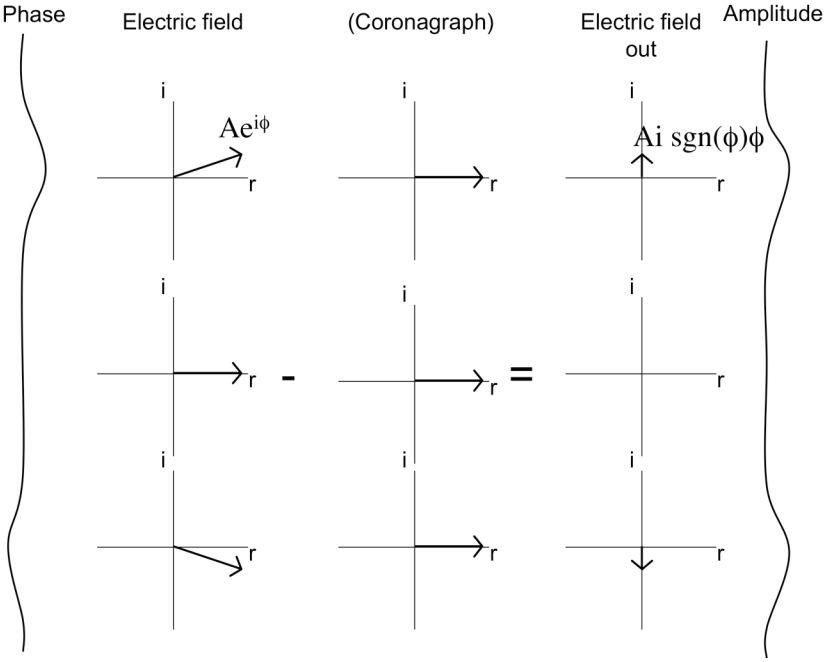

Figure 8: Illustration of wavefront propagation through a coronagraph. On the left, we input a wavefront with a uniform amplitude and a small phase error. In the next column we show the complex electric phasor associated with this at three points, one where the wavefront is flat and two where the wavefront has a positive and negative phase error. The act of passing through a perfect coronagraph is similar to the subtraction of the DC component of this electric field (more precisely, the electric field convolved with the Fourier transform of the occultor function.) As a result, for small phase errors the electric field becomes almost purely imaginary with an intensity proportional to the input phase error.

To overcome this limitation GPI incorporates a dedicated infrared wavefront sensor integrated with the coronagraph, known as the Calibration Interferometer or CAL subsystem. This wavefront sensor exploits the optical properties of the coronagraph to allow precise and accurate measurement of the pre-coronagraph wavefront. A perfect coronagraph acts to convert small phase errors into amplitude signals proportional to the original input phase (Figure 8). The resulting wavefront is almost pure imaginary with the sign (+i or –i) determined by the sign of the input phase error.

Consequently, the post-coronagraph wavefront sensor primarily needs to measure intensity and is almost completely insensitive to optical errors after the occulting mask. A post-occultor phase error will only rotate the electric field, with no affect on the measurable intensity. A simple camera would retain an ambiguity as to the sign of the input phase – the GPI system needs to recover the phase of its wavefront with only 90 degree accuracy to resolve this ambiguity.

GPI's high-order calibration interferometer (HOWFS) uses a portion of the on-axis light that passed through the coronagraph occultor, further spatially filtered, to make a spherical reference wavefront. A beamsplitter removes 20% of the off-axis science light, which is then interfered with the reference wavefront and imaged onto a commercial InGaAs camera. This interferometer is sensitive only to those spatial frequencies not blocked by the occulting hole, i.e. periods greater than 2.6 cycles per aperture. Low-frequency aberrations, including slow tip/tilt (which must be maintained to an average accuracy of 1 miliarcsecond), are measured by a separate low-order wavefront sensor (LOWFS). The LOWFS is a near-infrared Shack-Hartmann sensor with 7 subapertures across the Gemini pupil, operating at a wavelength of 1.7 microns with a commercial InGaAs camera. The HOWFS uses a similar camera. The LOWFS provides updates to the pointing of the main AO system at 1 Hz; the reconstructed LOWFS and HOWFS wavefronts are sent as reference centroid offsets to the main AO system once per minute. The CAL system is further discussed in a separate paper.[20]

7. SCIENCE INSTRUMENT

Spectral data is crucial to a high-contrast AO system. First, true planetary companions can be distinguished from speckle artifacts or background objects through analysis of a 3-dimensional data cube[21 22], although in practice this is will be limited by the chromaticity of the wavefront aberrations in the system. Second, the greatest scientific reward will come from spectral characterization of detected planets, and long-slit spectroscopy is almost completely impractical in coronagraphic mode. An integral field spectrograph (IFS) is the ideal science instrument, producing a 3-dimensional data cube with spectral information for every pixel in the field of view.

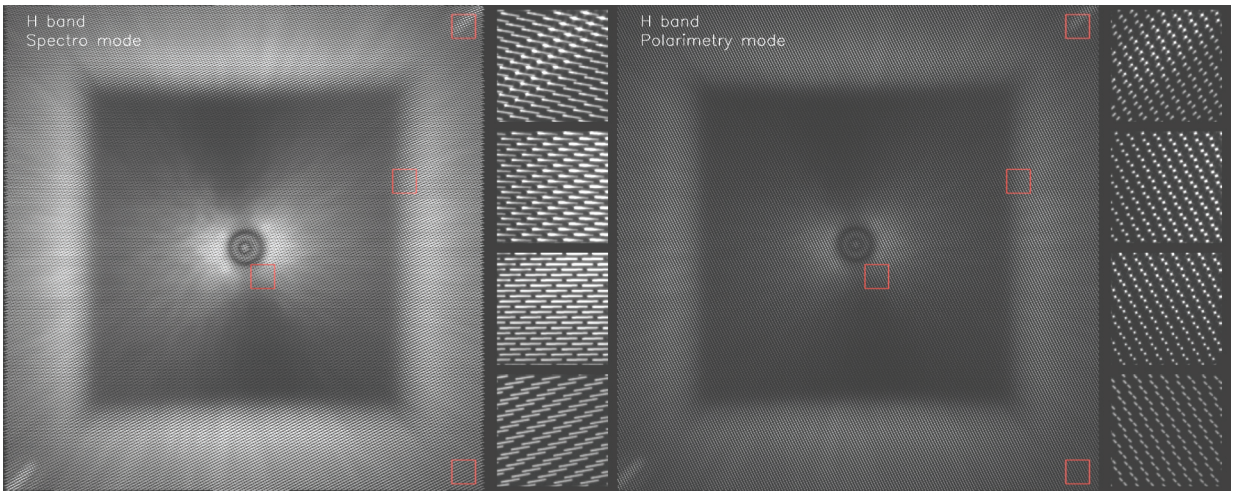

Figure 9: Raw integral field spectrograph images as seen by the IR array. Left: spectral mode, with individual R~45 spectra 16 pixels long. Right: Polarimetry mode, with each spectrum replaced by two images in the orthogonal polarizations.

GPI's IFS is a lenslet-based design, similar to the TIGER or Keck OSIRIS instruments. These use a grid of lenslets in the focal plane to dissect the image into a sparse grid of dots (essentially re-imaged telescope pupils) with enough space between them that the spectra can then be dispersed. For GPI's low-resolution (R~45 at *H* band), the disperser element is a prism. This gives a resolution that varies slightly in other spectral bands, from R~34 in Y band (0.95-1.14 μm) to R~70 in K band, which we divide into two smaller filters (1.90-2.19 μm and 2.13-2.40 μm). Individual spectra are 16 pixels long and separated by 4.5 pixels from their neighbors to reduce crosstalk to acceptable levels. The spatial sampling is 0.014 arcseconds per pixel. This gives a field of view of 2.8x2.8 arcseconds on a HAWAII 2RG detector.

In polarimetric mode, the spectral prism is replaced with a Wollaston prism that separates the two orthogonal polarizations from each lenslet onto on the final detector. A quarter-wave-plate modulator is located outside the dewar.

Vibration is a major concern for GPI. To reduce induced motions, the IFS uses a pulse-tube cooler manufactured by QDrive rather than a traditional Gifford-McMahon cooler. The QDrive is completely self-contained – no off-telescope

compressor. It produces ~20 watts of cooling at operating temperature and dissipates ~500W of heat, which will be removed by glycol circulation.

8. MECHANICAL DESIGN

GPI's mechanical design is broken up into two levels. An outer External Frame Structure (EFS) provides environmental protection and supports the external electronics racks. Inside, a Flexure Sensitive Structure (FSS) connects the individual subsystems in the optical path. The AO subsystem is supported on a custom-cast aluminum optical bench. The IFS and CAL units are held by a truss structure. The EFS and FSS connect to a mounting plate (MSS) that in turn connects to the Gemini Instrument Support Structure.

We have carried out extensive FEA modeling to determine the optical flexure of the system induced by gravitational, thermal, or vibration disturbances. Some of these are discussed in the context of integrated modeling in a separate paper. Typical alignment tolerances for GPI's various pupil planes are 0.5% of their diameter (~50 microns), maintained through stiff design, open-loop steering, and closed-loop tracking of the Gemini input pupil.

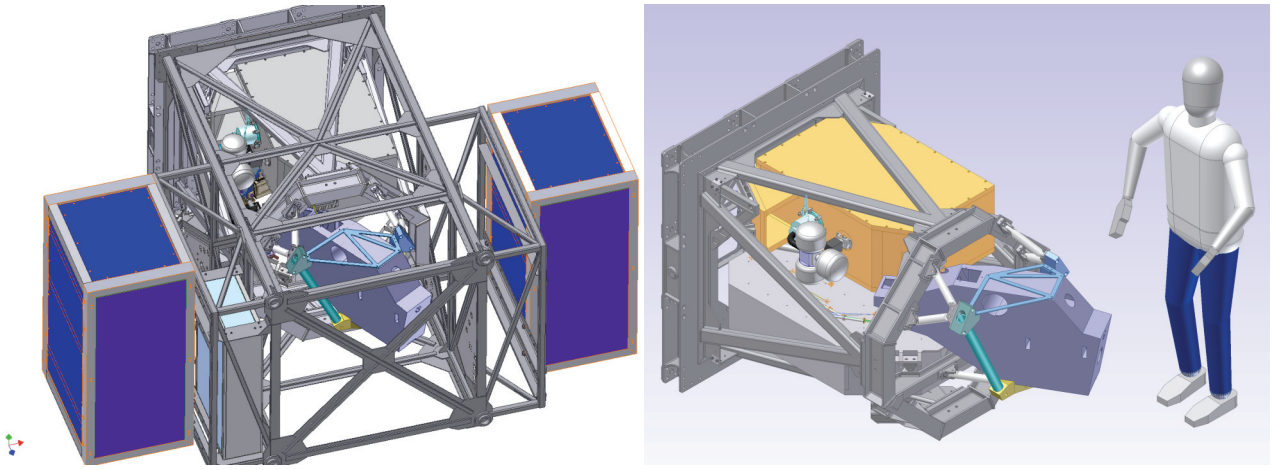

Figure 10: Mechanical design of the Gemini Planet Imager. Left: GPI with its covers removed, showing the outer EFS and electronics racks and the inner FSS. Right: Flexure Sensitive Structure (FSS) with the optical subsystems. The IFS is the yellow dewar at top; the CAL interferometer is inside the blue box at right; the AO subsystem is mounted on the grey optical bench at bottom. The square plate on the left mounts to the Gemini Cassegrain Instrument Support Structure.

9. PERFORMANCE MODELING

GPI uses a hierarchy of models to evaluate instrument performance. The adaptive optics system is modeled with a full dynamic AO model including multilayer translating frozen-flow atmosphere screens, physical optics modeling of the wavefront sensor, and control loop dynamics and delays. Output phase screens are fed at multiple wavelengths through a coronagraph model using a semi-analytic direct Fourier transform technique for high-resolution to produce simulated point spread functions. Simulating a one-minute exposure with this software requires ~200 CPU-hours of computer time.

Since many GPI quasi-static effects are only apparent in exposures of ten minutes or longer, we use a separate model to quantify quasi-static errors. The current version of this model uses full Fresnel propagation through every optic in the system, including optical surface and reflectivity errors, finite optics sizes, MEMS surface effects, and dust on individual optics. The results of the two simulations can then be fed through a SSDI multi-wavelength imaging pipeline (normally a scaled three-wavelength double-difference, DD) to evaluate final contrast. As can be seen in Figure 12, while atmospheric speckle noise is strongly attenuated by multi-wavelength processing, quasi-static speckle noise is only removed by ~2 magnitudes. Nonetheless, GPI achieves its contrast goal of being photon noise limited for R>5 λ/D.

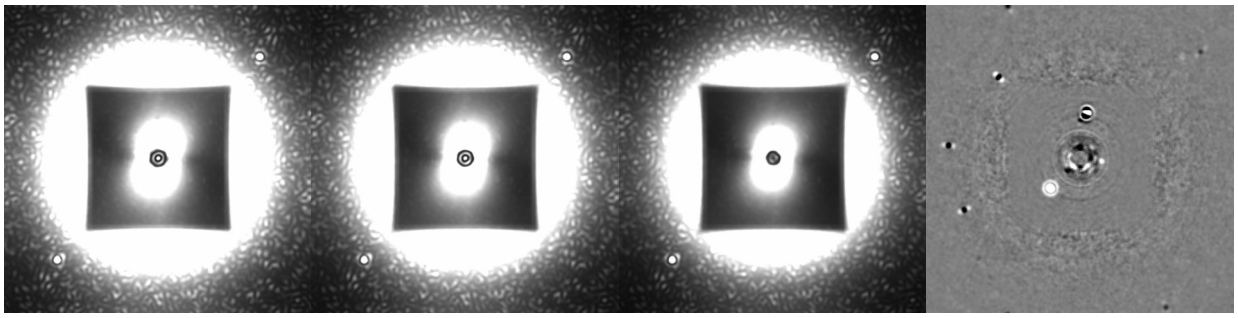

Figure 11: Simulated 1-hour exposure GPI images at 1.48 microns, 1.57 microns, and 1.78 microns. Right: Simulated PSF after double-difference processing with point sources added. This image is shown with a linear gray scale between -5E-7 and 5E-7 of the PSF peak (after convolution by the aperture). The object north of the star is a background object while the 2 objects south and west of the star are 2 planets. The one located south-east of the star is a 4 Mjup/580K planet while the one west of the star is a 1 Mjup/330K planet. Dark spots outside the dark hole are dust artifacts.

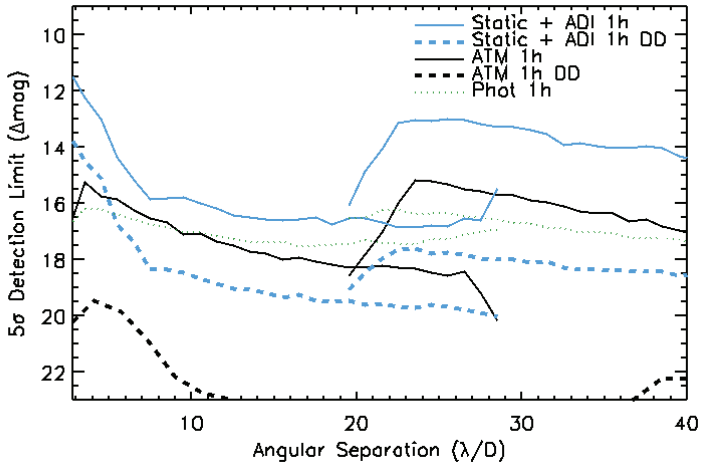

Figure 12: Simulated GPI contrast in a single R=45 spectral band at 1.60 μm in a 1-hour exposure of a *I*=6 mag. target star. Solid lines show contrast from internal static aberrations and atmospheric speckle noise; angular differential imaging (ADI) is assumed to provide only rotational averaging with the parallactic rotation of the science field. The dashed lines show contrast after a double-difference processing of three wavelength channels. The dotted line shows the photon noise in a single spectral channel. Overlapping lines show the radial average contrast inside and outside the square dark hole. GPI simulations for Gemini South use a r0=14 cm atmosphere. λ/D=0.04 arcseconds.

10. CONCLUSIONS

Designing a coronagraphic AO system for direct detection of extrarsolar planets requires an integrated approach to setting performance requirements and system modeling. Simulations show that GPI will achieve its goal of contrast ~10-7 from 0.2-0.8 arcseconds. GPI has passed its Critical Design Review (May 2008) and is beginning the construction phase. After individual subsystems are completed and tested, system-level integration and test will begin at UC Santa Cruz in early 2010, and first light should occur on the Gemini South telescope in early 2011.

ACKNOWLEDGEMENTS

The GPI team would like to thank the staff of the Gemini Observatory for their collaboration on the design of our instrument. This work was performed under the auspices of the U.S. Department of Energy by Lawrence Livermore National Laboratory in part under Contract W-7405-Eng-48 and in part under Contract DE-AC52-07NA27344. We also acknowledge support from the Natural Science and Engineering Council of Canada. The Gemini Observatory is operated

by the Association of Universities for Research in Astronomy, Inc., under a cooperative agreement with the NSF on behalf of the Gemini partnership: the National Science Foundation (United States), the Particle Physics and Astronomy Research Council (United Kingdom), the National Research Council (Canada), CONICYT (Chile), the Australian Research Council (Australia), CNPq (Brazil), and CONICET (Argentina)

REFERENCES

[1] Burrows, A., et al., "A nongray theory of extrasolar giant planets and brown dwarfs", Ap.J. 491, 856 (1997)

[2] Lafreniere, D., et al., "The Gemini Deep Planet Survey", Ap.J., 670, 1387 (2007)

[3] Marley, M., et al, "On the luminosity of young Jupiters", Ap.J. 655, 541 (2007)

[4] Soummer, R., et al., "Speckle noise and dynamic range in coronagraphic images", Ap.J. 669, 642 (2007)

[5] Trauger, T, & Traub, W., "A laboratory demonstration of the capability to image an Earth-like extrasolar planet", Nature 446, 771 (2007)

[6] Give'on, A., et al., "The electric field conjugation: a broadband correction algorithm for high-contrast imaging systems", Proc. SPIE 7010-136 (2008)

[7] Marois, C., et al., "An end-to-end polychromatic Fresnel propagation model of GPI", Proc. SPIE 7015-64 (2008)

[8] Dunn, J., et al., "Gemini planet imager autonomous software", Proc. SPIE 7019-37 (2008)

[9] Macintosh, B., and Poyneer, L., "Spatially filtered wavefront sensor for high-order adaptive optics", JOSA A 21, 810 (2004)

[10] Poyneer, L., and Veran, J.-P., "Optimal modal Fourier-transform wavefront control", JOSA A 22, 1515 (2005)

[11] Poyneer, L., Macintosh, B., and Veran, J.-P., "Fourier transform wavefront control with adaptive prediction of the atmosphere", JOSA A 24, 2645

[12] Cornelissen, S., Bierden, P., and Bifano, T., "A 4096 element continous facesheet MEMS deformable mirror for high-contrast imaging", Proc. SPIE 6888, p68880V

[13] Hill, A., "Stable flexure mounting of a MEMS deformable mirror for the Gemini Planet Imager", Proc. SPIE 7018-52 (2008)

[14] Soummer, R., "Apodized Pupil Lyot Coronagraphs for Arbitrary Telescope Apertures", Ap.J. 618, L161 (2005)

[15] Sivaramakrishnan, A., & Oppenheimer, B., "Astrometry and photometry with coronagraphs", 2006 Ap.J. 647, 620

[16] Marois, C., et al., "Accurate astrometry and photometry of saturated and corongaphic point spread functions", 2006 Ap.J. 647, 612

[17] Kern, B., private communication

[18] Genet, C., and Ebbesen, T.W., "Light in tiny holes", Nature 445, 39 (2007)

[19] Thomas, S., et al., "Testing the APLC on the LAO ExAO testbed", Proc. SPIE 7015-238 (2008)

[20] Wallace, J.K., et al., "Postcoronagraph wavefront sensing for the Gemini Planet Imager", Proc. SPIE 7015-243 (2008)

[21] Marois, C., et al., "Efficient speckle noise attenuation in faint companion imaging", PASP., 112, 91 (2000)

[22] Sparks, W., and Ford, H., "Imaging spectroscopy for extrasolar planet detection", Ap.J. 578, 543 (2002)